Ni/La₂O₃ catalysts for dry reforming of methane: Effect of La₂O₃ synthesis conditions on the structural properties and catalytic performances

M. Grabchenko [a,1], G. Pantaleo [b,1], F. Puleo [b], O. Vodyankina [a,**],
L.F. Liotta [b,*]

[a] Tomsk State University, 36, Lenin Ave., Tomsk, 634050, Russia
[b] Istituto per lo Studio dei Materiali Nanostrutturati (ISMN)-CNR, Via Ugo La Malfa, 153, Palermo, 90146, Italy

HIGHLIGHTS

- Two La₂O₃ oxides were prepared with citric acid method with and without NH₃.
- La(OH)₃ was encapsulated into the core of large La₂O₃ aggregates at pH ~2.
- Ni(NO₃)₂ solution partially diffused inside the support (pH~2) to form NiO.
- La₃Ni₂O₆ was the main Ni precursor formed on the support prepared with NH₃.
- Small Ni NPs tightly connected with La₂O₃ were observed after La₃Ni₂O₆ reduction.

GRAPHICAL ABSTRACT
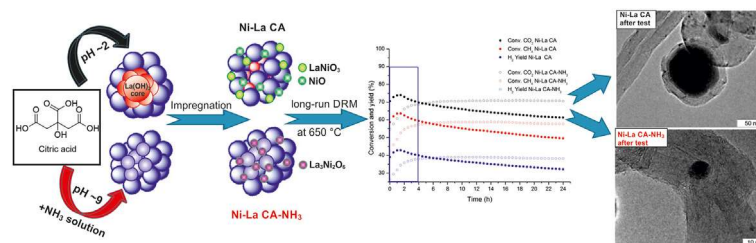
ARTICLE INFO

ABSTRACT

10 wt%Ni/La₂O₃ catalysts for dry reforming of methane (DRM) were synthesized by wetness impregnation of lanthana supports prepared using sol-gel citric method with and without NH₃ addition (Ni–La CA-NH₃ and Ni–La CA, respectively). The support preparation conditions affect the nature, phase composition, and distribution of Ni phases (LaNiO₃, NiO and La₃Ni₂O₆). The gradient temperature DRM tests (400–800 °C) reveal higher catalytic activity of Ni–La CA (at 650 °C, X(CO₂) = 65.7%, X(CH₄) = 54.6%, H₂/CO = 0.71). The Ni–La CA-NH₃ shows higher stability (at 650 °C and 24 h, X(CO₂): 73.7% => 76.4%, X(CH₄): 64.7% => 64.6%, H₂/CO: 0.77 => 0.72). For both catalysts, La₂O₂CO₃ phase is formed after long run tests at 650 °C 24 h, with the greater TGA weight loss and stronger deactivation being observed for Ni–La CA. The H₂-reduced Ni La CA-NH₃ features ultrasmall (1–2 nm) Ni NPs

$LaNiO_3$
NiO
$La_3Ni_2O_6$ phases

strongly interacting with the support. Catalyst nature affects the amount of carbon coke formed.

Introduction

The growing demand of the society in energy as well as the need of rational use of natural resources cause a profound interest of researchers to production of renewable energy sources. Catalytic technologies (selective oxidation, dry and steam reforming, etc.) are considered promising methods of biomass conversion into valuable products of fine organic synthesis (including the products of syngas conversion) and ecofriendly fuels (in particular, hydrogen). Great attention of both academia and industry is attracted by the processes of dry reforming of methane.

The dry reforming of methane (DRM) is a chemical process comprising conversion of methane and carbon dioxide, known as the abundant greenhouse gases, to syngas (hydrogen and carbon monoxide), with a H_2/CO molar ratio of 1:1. As a result, this process has the potential to mitigate the environmental challenges associated with greenhouse gases emissions and to convert biogas and natural gas into syngas. The syngas is used to produce a large number of products such as paraffins and oxygenates within the Fischer-Tropsch process. DRM is highly endothermic ($\Delta H°_{25°C} = 247$ kJ/mol) and normally requires temperatures above 700 °C to suppress the reverse water gas shift reaction (RWGS) and coke formation from the Boudouard reaction to attain good conversion levels [1].

Different catalysts have been proposed in the literature for the DRM process that contain noble metals, spinels, perovskites, mesoporous materials, etc. [2—5] Ni-based catalysts found the largest application due to their relatively low cost and high availability [1,6—9]. However, supported nickel catalysts have two main drawbacks: they are prone to sinter under high temperatures and suffer from severe coke deposition. Coke formation mainly originates from the Boudouard reaction and CH_4 decomposition. Thus, several carbon species are formed in the DRM process, such as atomic carbon (surface carbide) C_α (200—400 °C), polymeric amorphous films, C_β (250—500 °C), carbon of nickel carbide, C_γ (150—250 °C), vermilike filamentous carbon, C_v (300—1000 °C), graphite (crystalline) plated films, C_c (500—550 °C) [7]. Some carbon species reduce the catalyst activity, while other have no impact.

Noble metals (Rh, Ru, Pt, Ir, Pd, etc.) are also used in the DRM process and show higher resistance to coke formation compared to Ni-based catalysts [6,10]. However, their cost exceeds the one of the Ni-based catalysts. The temperature of the process performance is also significantly higher compared to Ni catalysts. Thus, noble metals are usually used as promoters for Ni-based catalysts that increase the stability to deactivation.

Al_2O_3, La_2O_3, MgO, V_2O_5, ZrO_2, Y_2O_3, etc. are the most widely used supports [11—21]. As a rule, supports with acidic surface are not useful for DRM process due to coke deposition [22]. Lanthana-supported Ni catalysts are actively studied due to high stability under DRM conditions, thanks to the formation of $La_2O_2CO_3$ species yielding $Ni—La_2O_2CO_3$ interfaces where the oxycarbonate interacts with the coke formed [23—25]. Moreover, being a basic support, La_2O_3 facilitates adsorption and activation of CO_2. Besides neutralization of acidity, the addition of La as a promoter usually results in the following effects: (1) stabilization of textural and structural properties of support, (2) improvement of catalytic properties by small metal particles and active surface, (3) suppression of coke formation and improving the stability [26]. Khoja et al. [27—29] reported $Ni/La_2O_3—MgAl_2O_4$ system tested in a cold plasma dielectric barrier discharge (DBD) reactor. The irregular structure of $MgAl_2O_4$ was changed into flakes upon incorporation of web-like La_2O_3 that also strengthened the metal-support interaction and improved catalyst basicity.

It is well known that the chemical and structural properties of catalysts, including the phase composition, the particle sizes, the distribution of active components play a significant role in activity and stability and the preparation conditions strongly affect such properties. Concerning Ni catalysts for dry reforming, investigations devoted to the improvement of activity and stability to coke poisoning are considerably growing in the last years. Most of them are based on the development of new efficient synthesis routes able to control the nature of Ni precursors together with their distribution on the support surface. The investigation of structure—activity relationship in Ni/La_2O_3 catalysts is attracting great attention. Xu et al. [30] showed that the preparation method influenced the features of the $Ni—La_2O_2CO_3$ interface, thus, enhancing the catalyst performance. The supports significantly differed in bulk structure that affected the strength of interaction of NiO/Ni and La_2O_3.

Nowadays, catalyst precursors with perovskite structure, especially lanthanum nickelates, have gained enormous interest. Lanthanum nickelates have high reducibility and oxygen storage/release capacity that is peculiar of the perovskite-type oxides. Various techniques of $LaNiO_3$ preparation are known, such as sol-gel [31], combustion [32,33], hydrothermal [34], microwave heating [35], molten salt [36], mechanochemical synthesis [37] and so on. As a rule, the main precursors used for preparation of $LaNiO_3$ and generally for La-containing perovskites are nitrates, oxalates and carbonates. Several researches have been carried out using nickel NPs formed in the course of reduction of $LaNiO_3$ perovskite used as catalyst precursors [38,39]. Recently, Bonmassar et al. [40] unravelled the phase structural dynamics showing polymorphic changes in $LaNiO_3$ structure at temperatures up to 620 °C during the DRM process that followed the raw: rhombohedral $LaNiO_3$ — cubic $LaNiO_3$ — triclinic $LaNiO_{2.7}$ and monoclinic $LaNiO_{2.5}$. The latter phase decomposed into the Ruddlesden-Popper phase La_2NiO_4 exhibiting moderate activity that at 670 °C transformed into metallic Ni NPs and monoclinic $La_2O_2CO_3$ to improve the DRM activity.

G.S. Gallego et al. in Ref. [41] showed that catalysts prepared by perovskite-type precursors exhibited higher activity and stability in comparison with Ni/La$_2$O$_3$ catalyst prepared by classical wet impregnation method. The achievement of highly dispersed active metal NPs on La$_2$O$_3$ surface is a significant challenge for Ni/La$_2$O$_3$ catalysts due to the limited surface area of lanthanum-based oxides [42]. Indeed, the increase in the Ni loading enhances the CH$_4$ and CO$_2$ conversion, however, high Ni loading involves low dispersion of the active sites with consequent fast carbon deposition and catalyst deactivation.

An effective solution of this problem may be the targeted formation of nickel particles through the reduction of dispersed lanthanum nickelates NPs on the surface of La$_2$O$_3$ with saving of simple preparation techniques (i.e wet impregnation as an available method) and low Ni loadings. The preparation method of La$_2$O$_3$ supports used in the present work consists of a sol-gel procedure based on the use of citrate solutions. Citric acid is a very effective chelating agent, which can take various deprotonated appearances (CitH$_3^-$, CitH$_2^{2-}$, CitH^{3-}, Cit^{4-}) in solution, depending on pH. This preparation method can improve the reactivity providing that the solution turns into the solid without any fractional precipitation. The La^{3+} solubility and the dissolution rate increased by molar excesses of citric acid. Under such conditions, La citrate solutions segregated precipitates at pH ~1–4 [43].

Based on Predoana et al. in Ref. [44], the mechanism of gelation of lanthanum nitrate containing citrate complex strongly depends on pH and largely determines the path of nucleation. At pH ~ 2–3 the aqua-cations of La^{3+} are formed during the processes of dissociation and solvation, after that a heteropolynuclear amorphous complex is formed where the carboxylic groups of the citric acid act as monodentate ligands [44].

The structure of the lanthanum citrate complex should change with an increase in the pH value up to 8–10. In presence of an alkaline agent, such as ammonia, OH$^-$ species (generated in aqueous solution by hydrolysis of NH$_3$) take part in the coordination sphere of the La^{3+}-citric complex. Moreover, at basic pH value, the carboxylic groups of the citric acid act as bridging ligands [44]. Therefore, addition of ammonia is expected to change the composition and size of the heteropolynuclear complexes participating in the formation of the gel. Consequently, the phase composition and textural properties of the sample prepared at pH ~8–9 should differ from those of the support prepared at pH~2. We also expect that the differences in phase composition and properties of the supports may influence significantly the nature and distribution of Ni particles on the catalyst surface.

Various lanthanum-citrate compounds have been studied in the latest years. Lanthanum citrate trihydrate was used as an intermediate in the preparation of a suitable lanthanum precursor [45]. In Ref. [44], the authors studied the gelling process of aqueous lanthanum-cobalt-citric acid complexes, while in Ref. [46] water-soluble dimeric lanthanum and cerium citrates and malates complexes formed in presence of ethylenediaminetetraacetate, were investigated. However, as far as we know, no studies on the effect of ammonia addition, during sol-gel citrate method, on the textural properties and structural features of La$_2$O$_3$ supports and the corresponding Ni catalysts have been explored up to now.

In the present work, two La$_2$O$_3$ oxides were prepared by sol-gel method in presence of citric acid in acidic (pH ~2) and basic (pH ~ 9) conditions. Then, Ni was deposited on the above quoted oxides, by wetness impregnation, after calcination and reduction in H$_2$/Ar flow the resulting Ni catalysts were characterized by several techniques (namely, XRD, TPR, TGA, Raman and TEM HR) and investigated in the DRM reaction.

Experimental

Preparation of support and catalysts

All the chemicals were Sigma- Aldrich of analytical grade (purity ≥98.5%) and used directly without any further purification. La$_2$O$_3$ supports were synthesized by a sol–gel method using citric acid (C$_6$H$_8$O$_7$·H$_2$O) as complexing agent. La(NO$_3$)$_3$·6H$_2$O was used as La precursor. The salt was dissolved in a few mL of water under magnetic stirring. Citric acid was dissolved in water separately in round-bottomed three-neck flasks. Metal solution was added rapidly to citric solution under vigorous stirring and the molar ratio between C$_6$H$_8$O$_7$·H$_2$O and the total metal ion was 1.2 (pH of solution ~2). To synthesize another La$_2$O$_3$ support, the pH of the prepared solution was adjusted to 9 by adding aqueous ammonia. The solution in the round-bottomed three-neck flask was concentrated in an oil bath at 90 °C for around 3 h, then dried in oven at 120 °C for a 12h, recovered and calcined under static condition at 350 °C for 1h (5 °C/min) and then at 800 °C for 4 h (5 °C/min).

Ni (10%wt) was deposited by wetness impregnation of Ni(NO$_3$)$_2$·6H$_2$O over two La$_2$O$_3$ oxides prepared with and without adding NH$_3$ solution, the corresponding catalysts were labelled as Ni—La CA and Ni—La CA-NH$_3$, respectively. All Ni based catalysts were calcined at 600 °C during 2h.

Materials characterization

Specific surface area (SSA) and pore size distribution of the samples were determined by N$_2$ adsorption-desorption isotherms at −196 °C using ASAP 2020 Plus Micromeritics. The specific surface area was calculated using the Brunauer—Emmett—Teller (S$_{BET}$) method and the pore size distribution curves and pore volume were determined by the Barrett—Joyner—Halenda (BJH) method from the desorption branches of isotherms.

The XRD measurements of the calcined/reduced and spent samples were carried out with a Bruker D 5000 diffractometer equipped with a Cu $K\alpha$ anode in the range from 10 to 90° (2θ). The crystalline phase composition was established by using the ICSD (Inorganic Crystal Structure Database, FIZ Karlsruhe). The mean crystallite sizes of detectable Ni phases were calculated by applying Scherrer equation.

The catalysts were studied by temperature-programmed reduction (H$_2$-TPR) using Micromeritics Autochem 2950 HP apparatus equipped with a thermal conductivity detector (TCD). The H$_2$-TPR profiles were registered after oxidative pretreatment of the catalysts in the temperature-programmed

oxidation (TPO) mode from room temperature to up to 350 °C with holding for 30 min, then they were cooled down. The H_2-TPR analysis was carried out in the temperature range from 25 to 1000 °C with a heating rate of 10 °C/min, a flow rate of 30 mL/min (5 vol % of H_2 in Ar).

The TGA experiments were carried out with a TGA/DSC1 STAR system (Mettler Toledo) under air or N_2 flow by heating from 100 up to 1000 °C in order to evaluate the amount of carbon or carbonates species deposited on Ni catalysts after tests. The CO_2 evolution occurring during the TGA experiments was monitored by QM analyser (Balzers, Quadstar).

Raman spectra were recorded to understand the graphitic degree of coke on the spent catalysts. Raman spectra were registered at ambient condition using InVia confocal Raman microscope (Renishaw, UK).

The morphologies of the reduced and spent catalysts were studied by transmission electronic microscopy (TEM) using a JEM—2200FS microscope (JEOL, Japan) with an accelerating voltage of 200 kV. High-resolution transmission electron microscopy (HRTEM) and High-angle annular dark-field scanning transmission electron microscopy (HAADF-STEM) were used. The crystal lattice parameters were calculated by Fourier transform using the DigMicrograph (GATAN) software.

Catalytic tests

The activity tests were carried out in a U-shaped fix-bed reactor with an inner diameter of 12 mm in an electrically heated furnace. Before the reaction, 50 mg catalysts were pretreated with 5 vol%O_2/He at 350 °C during 30 min, and then reduced with 5 vol%H_2/Ar from room temperature up to 700 °C (heating rate 10°C min^{-1}) for 1 h.

The reagent gas mixture consisting of 15 vol% CH_4 + 15 vol % CO_2 in N_2 was passed over the catalyst with a flow rate of 50 mL/min. The gradient temperature tests in DRM were carried out by increasing the temperature from 400 to up to 800 °C (by steps of 50 °C, holding time was 30 min at a target temperature). After the catalytic run in the temperature range of 400—800 °C, the catalyst was left under the reaction mixture at 650 °C for 24 h in order to study the stability over time (long run tests).

The inlet and outlet gas compositions were analyzed by GC (Agilent 7890B) equipped with a DB-1 capillary column and a molecular sieve in order to follow the evolution of all the species (CH_4, CO, CO_2, H_2, O_2) using FID and TCD detectors.

Single tests by flowing only 15% CO_2 and 15% CH_4 in N_2 (50 mL/min) were performed using the same condition.

The conversion of the CH_4/CO_2 and the selectivity of the products were calculated as follows:

$$CO_2 \ conversion(\%) = \frac{(CO_2)_{in} - (CO_2)_{out}}{(CO_2)_{in}} \ 100;$$

$$H_2 \ yield(\%) = \frac{(H_2)_{out}}{(CH_4)_{in}} \cdot \frac{100}{2};$$

$$CO \ yield(\%) = \frac{CO_{in}}{(CH_4)_{in} + (CO_2)_{in}} \ 100;$$

$$H_2 \ selectivity(\%) = \frac{H_2}{2((CH_4)_{in} - (CH_4)_{out})} \ 100;$$

$$CO \ selectivity(\%) = \frac{CO}{((CH_4)_{in} + (CO_2)_{in}) - ((CH_4)_{out} + (CO_2)_{out})} \ 100.$$

Results and discussion

Characterization of calcined supports and catalysts

The prepared samples were characterized by N_2 adsorption/desorption, XRD and H_2-TPR techniques. Specific surface areas of the prepared supports and catalysts were calculated using the Brunauer—Emmett—Teller (S_{BET}) and the porosity was estimated by BJH methods. In Table 1 textural properties are listed. The La_2O_3 support prepared under acidic conditions (La_2O_3 CA) has S_{BET} = 9.0 m^2/g, cumulative pore volume = 0.055 cm^3/g and mean pore size = 8.2 nm, while the one prepared under basic pH conditions (La_2O_3 CA-NH_3) has S_{BET} = 15.2 m^2/g, cumulative pore volume = 0.058 cm^3/g and mean pore size = 7.4 nm. During the La_2O_3 preparation using ammonia, the citrate complex with lanthanum possesses structure with hydroxyl groups in inner sphere that led to the formation of a well dispersion of the dense particles of this support in the course of the calcination procedure at 800 °C. Thus, NH_3 addition during sol-gel synthesis generates a support of La_2O_3 with an increased specific surface area that, together with stability in relation of the water vapor action, may facilitate the dispersion of the metallic Ni particles.

After Ni deposition and further calcination, a slight further decrease of the specific surface area (SSA) (8.3 and 10.5 m^2/g) and of the pore volume (0.047 and 0.052 cm^3/g) occurs for Ni—La CA and Ni—La CA-NH_3 with respect to the lanthana oxides. Subtly higher mean pore size values were measured for both catalysts (8.5 and 9 nm, respectively).

The XRD method was used to evaluate the nature of the crystalline phases formed and to calculate the crystallite size according to Scherrer's equation. Fig. 1a and 1b shows the XRD patterns of the as-prepared supports and catalysts. Peaks attributed to La_2O_3 (ICSD #24693) and La(OH)$_3$ (ICSD #200090) were detected in both supports calcined at 800 °C (Fig. 1a). The peaks attributed to La(OH)$_3$ were more intense in the case of the La CA support (see rectangle selected area), while the XRD patterns of La CA-NH_3 sample showed that ammonia addition favoured the La_2O_3 phase formation with respect to La(OH)$_3$. The crystallite sizes of La(OH)$_3$ and of La_2O_3 phases were estimated by Scherrer's equation for the two lanthana oxides calcined at 800 °C (see Table 1). The La CA sample was characterized by crystalline phases with sizes of 49 and 25 nm for La_2O_3 and La(OH)$_3$, respectively. In the case of La CA-NH_3 support the crystalline phases of La_2O_3 and La(OH)$_3$ were observed with rather smaller sizes (34.5 nm and 3 nm, respectively).

Fig. 1b shows diffraction patterns of the calcined catalysts. Generally, the Ni-based catalysts maintained the structure already discussed for the supports, moreover, Ni phases, such as LaNiO$_3$/La$_3$Ni$_2$O$_6$ perovskites and NiO were detected. From a

Table 1 — Textural properties of La CA and La CA-NH₃ and Ni supported catalysts (as calcined).

Samples	SSA (m²/g)	Mean pore size (nm)	Cumulative pore volume (cm³/g)	Crystallite size (nm)		
				La_2O_3	$La(OH)_3$	NiO
La CA	9.0	8.2	0.055	49.0	25.0	—
La CA-NH₃	15.2	7.4	0.058	34.5	3.0	—
Ni—La CA	8.3	8.5	0.047	nd	19.0	8.0
Ni—La CA-NH₃	10.5	9.0	0.052	20.0	15.0	nd
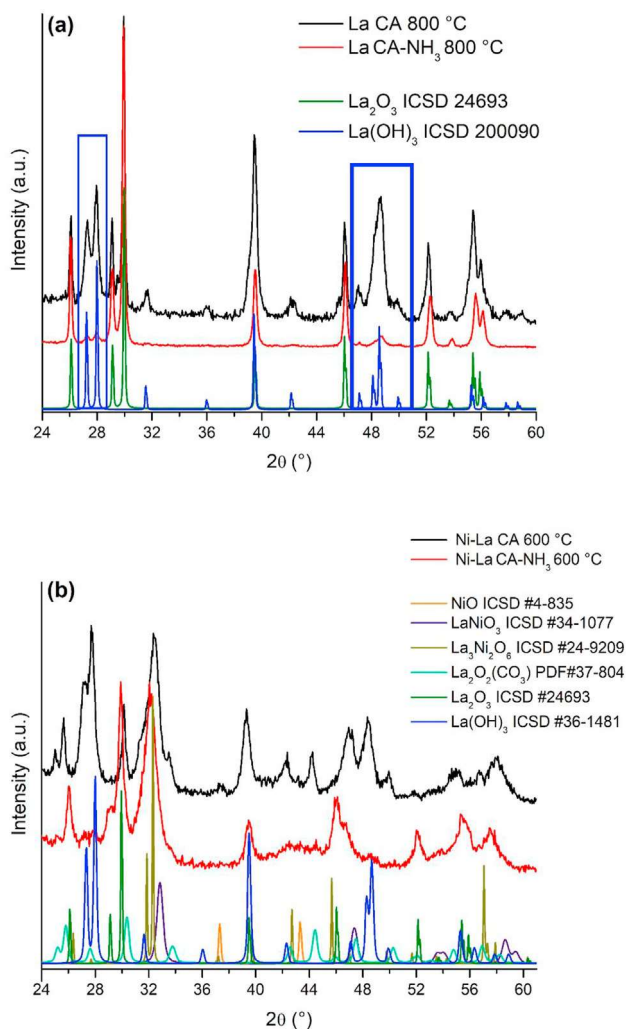
Fig. 1 — XRD patterns of the calcined supports (a) and catalysts (b).

careful analysis of Fig. 1b it results that Ni—La CA catalyst is characterized by mixture of $La_3Ni_2O_6$ (ICSD#24-9209) and $LaNiO_3$ (ICSD #34-1077) phases with most contribution of $LaNiO_3$, NiO (ICSD #4-835), $La_2O_2(CO_3)$ (PDF #37-804) and $La(OH)_3$ (ICSD #200090). In case of Ni—La CA-NH₃ catalyst, La_2O_3 (ICSD #24693), $La_3Ni_2O_6$ with shoulder of $LaNiO_3$ were the main phases along with $La_2O_2(CO_3)$ and $La(OH)_3$ as minor features.

The formation of lanthanum carbonates $La_2O_2(CO_3)$ is in agreement with the basic character of the lanthana oxide. Bernal et al. [47] showed that the nucleation of carbonated phase occurred during the wetting step, whereupon the

support can slowly take up further amounts of CO_2 by simple exposure to air. It is worth noting that for Ni—La CA sample, the reflection of La_2O_3 disappeared completely, and oxocarbonates with composition $La_2O_2(CO_3)$ (PDF #37-804) were detected. Moreover, the basic reflections for $La(OH)_3$ phase were maintained in the pattern of the Ni—La CA sample after the impregnation by Ni precursor solution and the subsequent calcination. According to the findings related to the supports, the reflections of $La(OH)_3$ phase in the pattern of the Ni—La CA were more intense in comparison with those for Ni—La CA-NH₃ sample. This fact was associated with the encapsulation of the $La(OH)_3$ inside the La_2O_3 aggregates for the La CA support. Encapsulation probably occurred during the first calcination when too large aggregates (49 nm) were formed at the stage of gel (at pH ~2). During the thermal treatment of the support, the external part of the aggregate dehydrated to yield La_2O_3 particles that were in close contact with each other. This hindered the dehydration of the internal part of the aggregate, and the $La(OH)_3$ was preserved in its core part. Such effects were observed for different systems. In Ref. [48] a significant shift of the temperature of decomposition of bismuth oxycarbonate phase towards high-temperature region was observed due to its encapsulation by SiO_2 layer. Such processes occurred during the thermal treatment of large particles of aluminum hydroxide when pseudoboehmite was formed in the internal part of the spherical particles due to the presence of vapor-phase water in the central part similar to the hydrothermal treatment conditions [49].

At the stage of impregnation of the Ni—La CA sample with the $Ni(NO_3)_2$, the solution partially penetrated into the La_2O_3 particles followed by the adsorption and diffusion of Ni^{2+} cations inside the subsurface layers of lanthana support. As a result, the excess of solution crystallized at the external surface of the support as $Ni(NO_3)_2$ and decomposition of the latter yielded NiO. An average crystallite size of NiO ~8 nm, as calculated by Scherrer's equation, was found for the Ni—La CA catalyst, while no diffraction peaks of NiO were observed for the Ni—La CA-NH₃ catalyst due to the stabilization of nickel as lanthanum nickelate phase ($LaNiO_3$ and $La_3Ni_2O_6$). Scheme 1 depicts the effect of NH₃ addition on the structural properties of La_2O_3 oxides and the corresponding Ni catalysts.
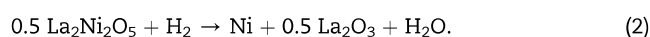
These data are in line with the slightly higher SSA of the La CA-NH₃ support allowing a better dispersion of the Ni nitrate precursor and confirm that the Ni—La CA-NH₃ catalyst retains better textural properties than Ni—La CA also in terms of La_2O_3 and $La(OH)_3$ crystallite sizes (see Table 1).

To study the reduction behaviour of the calcined catalysts, H₂-TPR experiments were performed. Fig. 2a shows the H₂-TPR profiles of the calcined catalysts, and Table 2 summarizes the H₂ consumption data and reduction temperatures. The
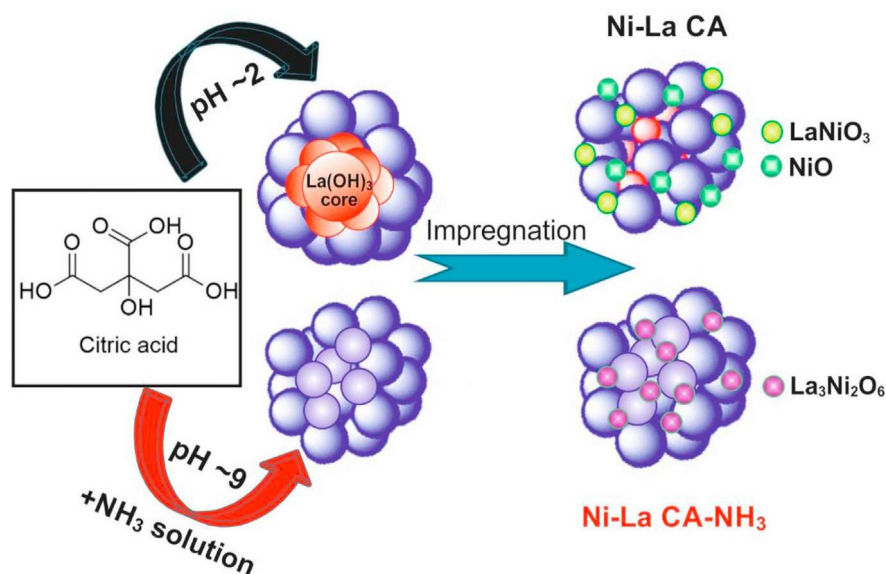
Scheme 1 — Effect of NH$_3$ addition on the structural properties of La$_2$O$_3$ oxides and the corresponding Ni catalysts.

TPR profiles of the Ni-based catalysts are characterized by two main consumption peaks. The low-temperature peaks, registered in the temperature range of 100–400 °C, are related to the reduction of larger NiO particles less interacting with the La$_2$O$_3$ support, while the high-temperature peaks at 450–750 °C were ascribed to the reduction of small NiO particles strongly interacting with the La$_2$O$_3$ support [50] and/or to the reduction of LaNiO$_3$ or La$_3$Ni$_2$O$_6$ particles [24,42,51]. It is noteworthy that in the case of Ni–La CA sample the consumption peaks in the region 100–400 °C are not symmetric, suggesting the presence of at least two peaks (see Fig. 2b) due to concomitant reduction of both Ni^{3+} and Ni^{2+} species or simultaneous reduction of nickel ions with a different chemical environment. In details, the peak at 275 °C was ascribed to the reduction of Ni^{3+} to Ni^{2+}, while the peak at 330 °C was assigned to the reduction of Ni^{2+} to Ni^0 [52]. By increasing the temperature, the broad peak centered at ~550 °C and the smaller one at 710 °C were attributed to the reduction of the NiLaO$_3$ phase according to the following reactions [53]:

$$LaNiO_3 + 0.5\ H_2 \rightarrow 0.5\ La_2Ni_2O_5 + 0.5\ H_2O, \tag{1}$$

$$0.5\ La_2Ni_2O_5 + H_2 \rightarrow Ni + 0.5\ La_2O_3 + H_2O. \tag{2}$$
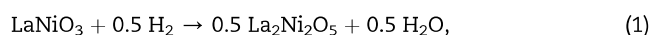
As already discussed for Ni–La CA, also in the case of Ni–La CA-NH$_3$ the reduction profile is characterized by main two peaks with reduction temperatures higher than those for Ni–La CA, suggesting higher strength of interaction between Ni species and the support. Moreover, the symmetric high-temperature reduction peak is shifted towards the higher temperature region by 55 °C (from 572 to 627 °C) for the Ni–La–NH$_3$ confirming the formation of lanthanum nickelate with different structure. According to the XRD data, the Ni$^+$/Ni^{2+} mixed-valent nickelate (La$_3$Ni$_2$O$_6$ phase) [54] was formed predominantly for Ni–La–NH$_3$, while the formation of the Ni^{3+} nickelate (LaNiO$_3$ phase) was formed for Ni–La CA sample.
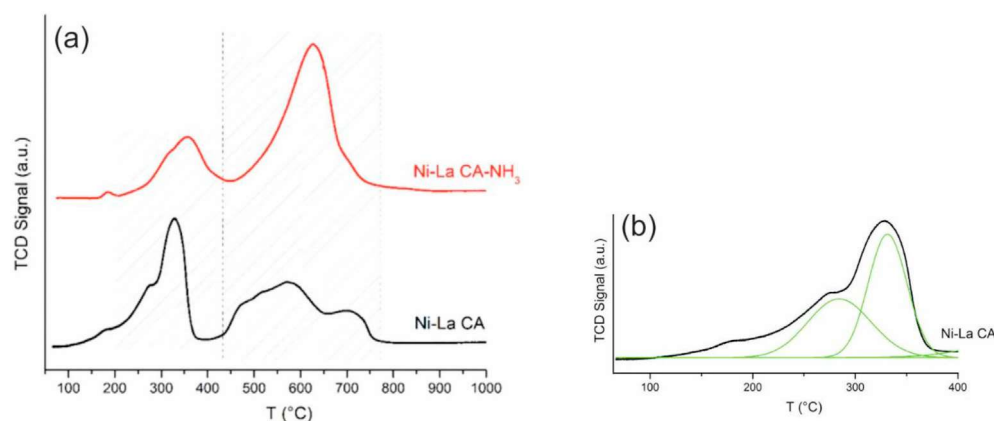
Fig. 2 — H$_2$-TPR profiles of the calcined catalysts (a), fitting of the TPR profile of Ni La CA in the low temperature range (50–400 °C).

Table 2 — Reduction temperatures and H₂ consumption registered in TPR experiments.

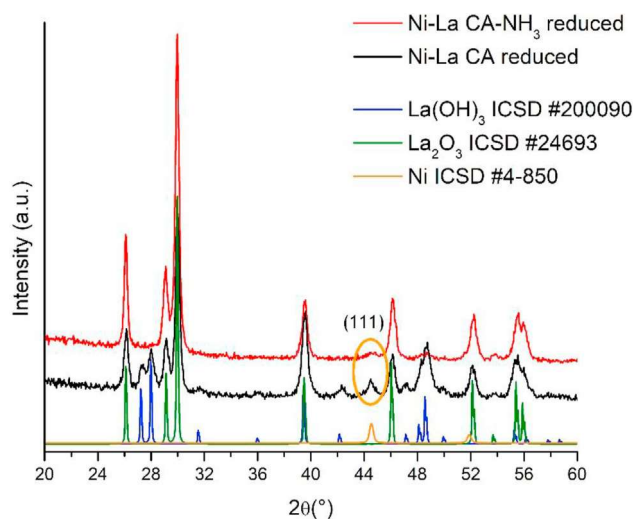| Samples	Reactions	Experimental H₂ consumptions (mL/g)	Theoretical H₂ consumptions (mL/g)
Ni–La CA	$Ni^{3+}/Ni^{2+} \rightarrow Ni^0$	20.9 (275, 330 °C)	41.7 ($Ni^{2+/0}$)
		40.2 (550, 710 °C)	
Total consumption (mL H₂/g)		61.1	41.7
Ni–La CA-NH₃	$Ni^{3+}/Ni^{2+} \rightarrow Ni^0$	10.9 (356 °C)	41.7 ($Ni^{2+/0}$)
		40.5 (627 °C)	
Total consumption (mL H₂/g)		51.4	41.7

Consequently, different Ni species with different oxidation states are stabilized over the lantana support, as a function of the preparation method. It is worth noting that for both catalysts the H₂ consumption listed in Table 2 is higher than the theoretical one required for reduction of Ni^{2+} confirming that Ni^{3+} cations are also present. Moreover, higher hydrogen consumption was detected for Ni–La CA suggesting higher amount of Ni^{3+} with respect to the Ni–La CA-NH₃.

Characterization of reduced catalysts

Before each catalytic test in DRM, the catalysts were pre-treated at 350 °C for 30 min in 5 vol% O₂/He flow and then at 700 °C for 1h in 5%H₂/Ar flow. In order to investigate the samples structure and morphology before the catalysis, the reduced catalysts were studied by XRD and TEM HR techniques.

Fig. 3 represents the XRD patterns of the reduced catalysts. In the XRD pattern of Ni–La CA-NH₃ after calcination at 600 °C and reduction treatment at 700 °C, the La₂O₃ was the only lanthanum-containing phase detected. Moreover, a weak and broad feature at ~44.4° 2θ ascribable to disperse metallic Ni particles was found. Conversely, in the case of Ni–La CA, both La₂O₃ and La(OH)₃ phases were identified along with a visible peak of metallic Ni corresponding to particles with mean size of ~20 nm as estimated by Scherrer's equation.

TEM HR analyses with a mapping technique were performed in order to characterize the elemental distribution patterns of the catalysts and thoroughly measure the Ni particle size distribution. Fig. 4 displays the HAADF image (a) of the reduced Ni–La CA catalyst with the corresponding La and Ni mapping distribution (Fig. 4b and c). Ni particles are present in both, aggregate (20–30 nm) and disperse forms (5–10 nm) (Fig. 4b). In the dashed circle (Fig. 4c), an aggregate of close Ni nanoparticles is observed. Moreover, for this sample, besides the La₂O₃ phase, also the Ni₂O₃ phase was detected as confirmed by FFT calculations (see S1). Therefore, in the catalyst Ni–La CA, upon reduction at 700 °C 1h, under 5 vol% H₂/Ar, not all the Ni oxidized species were reduced to metallic Ni.

For Ni–La CA-NH₃, nickel nanoparticles with relatively small sizes (1–2 nm) were detected (FFT in Fig. 5a), according to the broad peak registered in the XRD pattern. Such Ni particles are significantly smaller than in the case of Ni–La CA catalyst, moreover, they appear uniformly distributed over the support (Fig. 5b). Furthermore, some very small nickel particles (with sizes less than 1 nm) seem to be encapsulated into the La₂O₃.

Based on the so far reported XRD and TEM HR characterization data it results that Ni La CA contains crystallite size of NiO ~8 nm and, upon reduction at 700 °C for 1h under 5%H₂/Ar flow, a further increase in size up to aggregates of Ni metallic particles (20–30 nm), due to sintering, occurs. Conversely, Ni La CA-NH₃, thanks to the stabilization of nickel oxidized species, as lanthanum nickelate phase (LaNiO₃ and La₃Ni₂O₆) (see Scheme 1), features ultrasmall (1–2 nm) Ni NPs uniformly distributed and strongly interacting with the support.

Test of CH₄ decomposition and test of CO₂ activation over Ni catalysts

In order to get insights into the reaction mechanism, simple CH₄ and CO₂ temperature programmed tests were carried out. It was reported in the literature that the decomposition of methane occurred over Ni particles to yield highly reactive C_α species that can be further gasified by reactions with H₂O, CO₂, or H₂, while some methane is converted into the less reactive C_β, which may be stored on the catalyst surface [55]. Hence, it is important to study the catalysts in the methane conversion reaction to investigate the C–H bond activation and H₂ production as well as the contribution of this reaction to coke formation during the DRM process.

Fig. 6a, b shows catalytic test by flowing only 15%CH₄ in N₂. Both pictures show CH₄ consumption accompanied by the H₂ formation. The highest methane consumption and highest H₂ production (−43534 and 86884 ppm, respectively) were observed over the catalyst prepared without ammonia. This means that the methane decomposition reaction is predominant in the case of Ni–La CA catalyst.
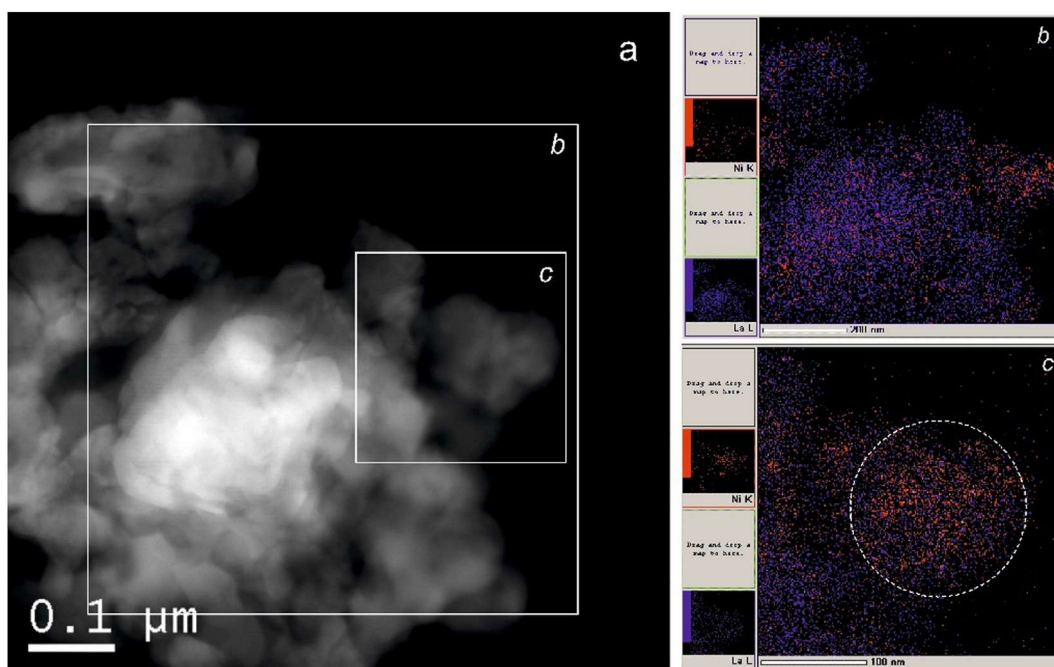

Fig. 3 — XRD patterns of the reduced catalysts.

Fig. 4 — HAADF image of Ni—La CA (a) with La—Ni mapping distribution (b, c) in the marked fragments.

Fig. S2 a presents the diffraction patterns of the Ni catalysts after CH_4 decomposition. It is noteworthy that the peak of metallic Ni and/or NiC at ~44.5° 2θ is well evident for the Ni—La CA along with the formation of carbon graphite mainly occurring for this sample (Fig. S2 b, a shoulder at ~26.3° 2θ). On the contrary for Ni—La CA-NH$_3$, the peak at ~44.5° 2θ is slightly visible suggesting the presence of metallic Ni particles well dispersed and/or a low content of NiC phase.

The study of the CO_2 activation was also carried out over the two Ni catalysts. Fig. 7 a,b shows the results of CO_2 test. Two peaks of CO_2 consumption were observed for both catalysts. For Ni—La CA catalyst, the low-temperature peak started at temperature above 400 °C, while for Ni—La CA-NH$_3$ catalyst this peak was observed at higher temperature (438 °C). In both cases the low-temperature CO_2 consumption corresponded to

lanthana carbonates formation, likely $La_2O_2CO_3$ species, according to the mechanism proposed by Verykios [25]. The high-temperature peak of CO_2 consumption with the corresponding CO evolution above 650 °C was attributed to the formation of the perovskite phase La_2NiO_4 as observed by the XRD characterization of the spent samples (see S3). For both spent catalysts, the La_2O_3, $La_2O_2CO_3$, La_2CO_5, and La_2NiO_4 were the main detected phases confirming high CO_2 chemisorption and reaction with both catalysts in the temperature range investigated.

To assess the coke formation after CH_4 and CO_2 tests, the TGA analyses were performed in the air atmosphere. The curves after CH_4 test show a little weight gain at ~450 °C that may be attributed to the oxidation of metallic Ni to NiO occurring under the air flow. Then, by increasing the
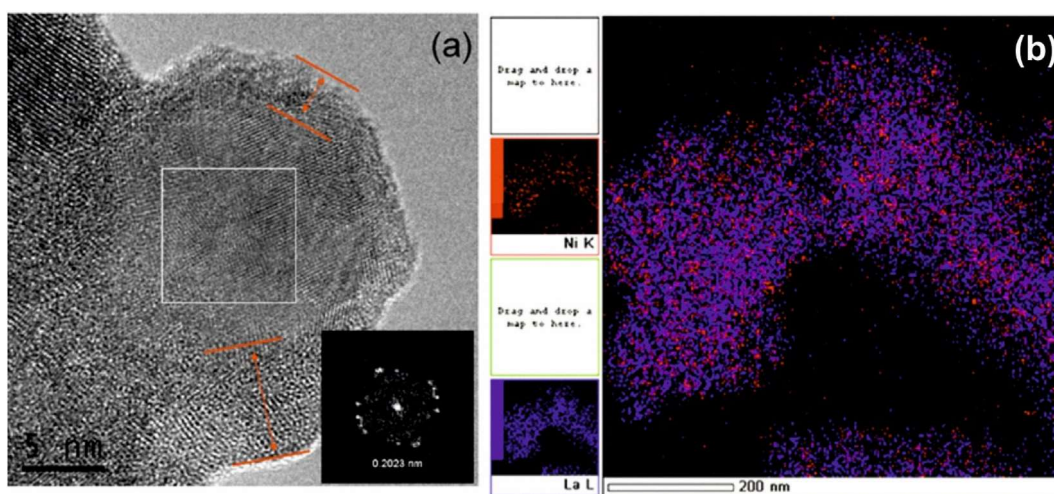

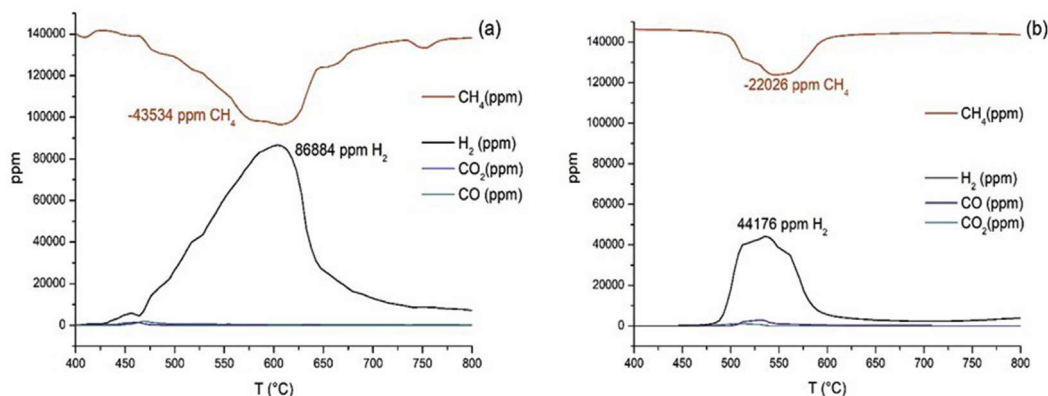**Fig. 5 — HR TEM image of Ni—La CA-NH$_3$ (a) with La—Ni mapping distribution (b) in the marked fragment.**

Fig. 6 — Test of CH_4 decomposition over Ni–La CA (a) and Ni–La CA-NH$_3$ (b).

temperature, the oxidation of carbon coke accumulated during the CH_4 decomposition occurs, with the consequent weight loss being equal to -14.8 wt% for Ni–La CA-NH$_3$ and to -25.8 wt% for Ni–La CA, respectively. The observed weight loss is accompanied by a concomitant CO_2 evolution. This trend is in agreement with the CH_4 decomposition tests shown in Fig. 6. In addition, for Ni–La CA-NH$_3$, the shape of the TGA curve and the high temperature of carbon oxidation suggest a slower oxidation process due to the presence of the graphitic carbon species for such sample. After the CO_2 test, we observe a low weight loss above 650 °C due to the decomposition of carbonates.

Fig. 8 shows the morphology of the carbon formed on the surface of Ni/La$_2$O$_3$ catalysts after methane decomposition. The carbon formed over these catalysts was observed to be of the filamentous type. From the TEM HR data, the highest carbon deposition was found on the Ni–La CA surface. As can be observed in Fig. 11a, b, c, the Ni particles migrated out of the support due to the growth of carbon fibers with a diameter of 20–50 nm. In addition, some Ni particles were encapsulated by the fibers. Fig. 8b shows that Ni particles with sizes of ~15 nm were located in the hollow channel, while Fig. 8c showed that Ni particle of ~10 nm were located at the tip of the fiber and encapsulated by graphene layers.

Conversely, the Ni–La CA-NH$_3$ catalyst after the CH_4 test is characterized by a relatively lower carbonization than Ni–La CA (see Fig. 8d, e, f). The catalyst surface contains mostly LaO$_x$ aggregates shown in Fig. 11d (EDX mapping is not shown). Differently from the Ni–La CA, only few Ni particles (12–15 nm) are removed from the surface and encapsulated by the thin carbon fibers having a diameter of ~20 nm (Fig. 8d and e). Fig. 8f shows the structure of the hollow channel of carbon fibers without any Ni encapsulations.

Raman spectroscopy was used to study the nature of the carbon deposits formed onto the spent catalysts. S5 shows the Raman spectra after CH_4 and CO_2 tests. The peaks at 1309 cm^{-1} and 1603 cm^{-1} correspond to a typical D (the Raman-allowed phonon mode E$_{2g}$ and involves out-of-phase intra-layer displacement in the graphene structure) and G bands (polycrystalline imperfect graphite), respectively. The peak positioned at around 2612 cm^{-1} (2D) is typically attributed to the graphite carbon. The relative intensity between the two peaks (I_D/I_G) provides information about the nature of carbon nanotubes and the extent of crystallinity of the carbon formed. Smaller I_D/I_G values indicate higher crystallinity due to higher contribution of the graphitized carbon [56,57]. The I_D/I_G ratio for the samples after CH_4 test equals to 2.36 and 1.82 for Ni–La CA and Ni–La CA-NH$_3$, respectively. Therefore, over Ni–La CA-NH$_3$, the carbon formed is more crystalline than for
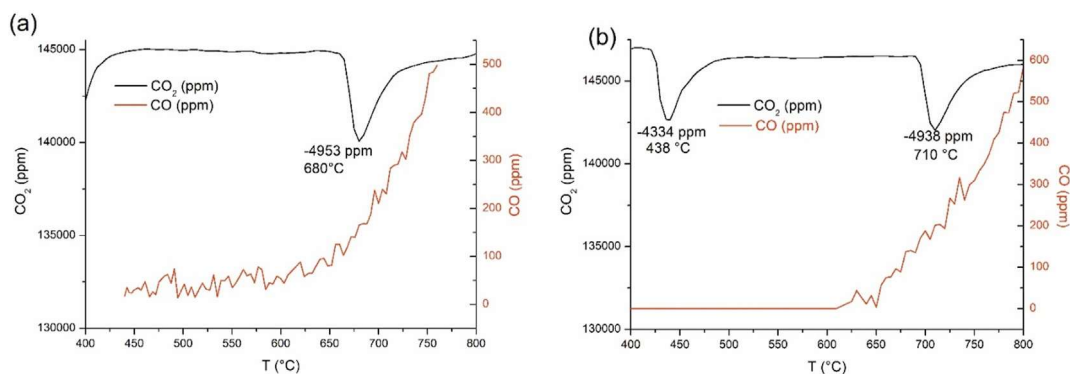

Fig. 7 — Test of CO_2 activation over Ni–La CA (a) and Ni–La CA-NH$_3$ (b).
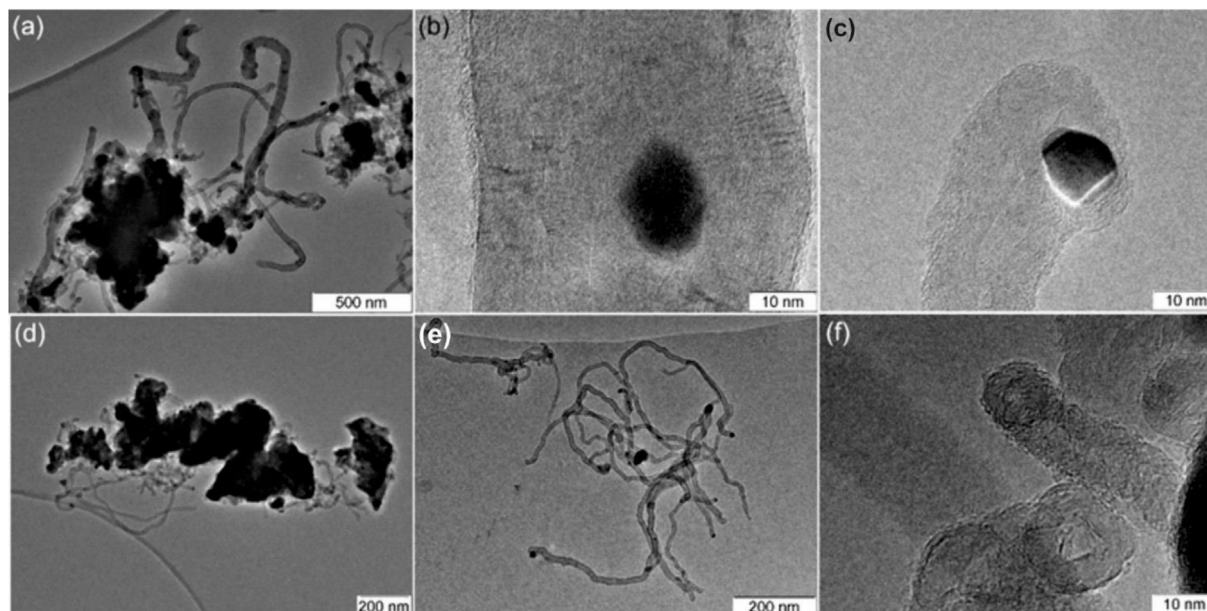
Fig. 8 — TEM HR images taken after CH₄ decomposition for Ni–La CA (a, b, c) and for Ni–La CA-NH₃ (d, e, f).

Ni–La-CA that is in accordance with the high carbon decomposition temperature detected in the TGA experiments (see S4). No carbon was observed after the CO_2 test.

Catalytic test of dry reforming of methane at gradient temperature

The DRM catalytic tests at gradient temperature performed between 400 °C and 800 °C reveals higher CO_2 and CH_4 conversion values for the Ni–La CA with respect to Ni–La CA-NH₃ (see Fig. 9a). In addition, the former catalyst shows higher H_2/CO ratio starting from 500 °C with values being quite close to the equilibrium ones [58]. In Table 3, the experimental values are listed and compared with equilibrium values from the literature [58]. In the entire range of temperature investigated. CO_2 conversion values were higher than the equilibrium in the range from 600 up to 800 °C. In agreement with the literature [59–61], higher CO_2 conversion could be due to the concomitant occurrence of the reverse WGS reaction

($CO_2 + H_2 \Leftrightarrow CO + H_2O$) and as well of CO_2 dissociation in CO and suprafacial oxygen, favoured by the surface basicity and as well to the direct reaction with carbon deposit according to the reverse Boudouard reaction ($C + CO_2 \Leftrightarrow 2CO$).

The reverse WGS reaction taking into account hydrogen consumption explains the observed H_2/CO ratios that are lower than equilibrium values (2.0–1.1). The ratio H_2/CO approaches 1 only near 800 °C, at these temperatures the CH_4 conversion is near the equilibrium, the CO_2 values being higher. Therefore, the CO_2 adsorption/conversion continues to be favourite with respect to the CH_4 decomposition, the dry reforming of methane becomes the main reaction by increasing the temperature.

Stability tests were carried out to investigate the performance of the catalysts over the long-time test. Fig. 10 presents the results of the DRM long run test performed at 650 °C during 24h in terms of CH_4 and CO_2 conversions and H_2 yield. The main catalytic results are summarized in Table 3 and compared with data recorded during the gradient
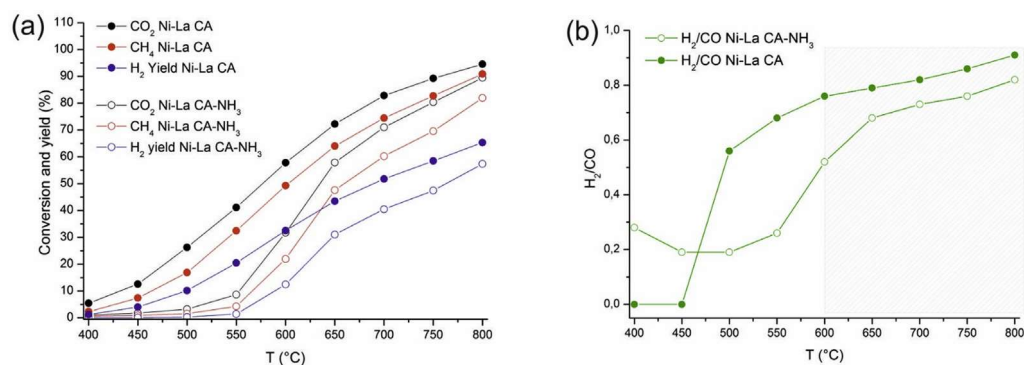

Fig. 9 — CO_2 and CH_4 conversion values (a) and H_2/CO ratio versus temperature (b) for Ni La-CA and Ni–La CA-NH₃ during DRM at gradient temperature.

| Table 3 — Main catalytic results during DRM tests (gradient temperature and long run tests) carried out over Ni/La$_2$O$_3$ catalysts. The equilibrium values according to Ref. [58] are reported for comparison.						
Sample		650 °C	700 °C	800 °C	Start long run 650 °C	End long run 650 °C
Ni—La CA-NH$_3$	Conv CO$_2$ (%)	55.8%	77.2%	94.1%	73.7%	76.4%
	Conv. CH$_4$ (%)	42.1%	65.1%	90.7%	64.7%	64.6%
	H$_2$ Yield (%)	26.9%	44.5%	65.4%	43.9%	39.7%
	H$_2$/CO	0.62	0.73	0.88	0.77	0.72
Ni—La CA	Conv CO$_2$ (%)	65.7%	80.0%	94.7%	71.7%	62.2%
	Conv. CH$_4$ (%)	54.6%	72.7%	93.2%	63.3%	50.0%
	H$_2$ Yield (%)	36.3%	49.7%	66.5%	43.2%	33.0%
	H$_2$/CO	0.71	0.8	0.9	0.77	0.67
Equilibrium values	Conv CO$_2$ (%)	54.5%	66.3%	88.6%	—	—
	Conv. CH$_4$ (%)	87.4%	91.5%	96.3%		
	H$_2$ Yield (%)	64.9%	75.9%	90.6%		
	H$_2$/CO	2.0	1.5	1.1		

temperature tests (see Fig. 9). During the long run, the catalyst Ni—La CA after a short induction period of 1h achieved the maximum conversion values and H$_2$ yield, then after ~2 h of reaction started slowly to continuously decrease the activity indicating that the deactivation process is running. On the contrary, Ni—La CA-NH$_3$ catalyst showed a better stability in long run test despite its initial low activity in the DRM. The lower catalytic activity of Ni—La CA-NH$_3$ can be due to very small Ni particles interacting with the support, being consistent with the TPR, XRD, and TEM HR characterizations (see Figs. 2, 3 and 5). Such small Ni particles are likely activated during the first 4h under the reaction mixture, reaching an optimum ensemble size of active Ni sites for the reaction. In addition, other phenomena may be responsible for the observed induction period and the subsequent active and stable performance for the Ni—La CA-NH$_3$ catalyst. Indeed, as

proposed by Verykios [25], the formation of the stable La$_2$O$_2$CO$_3$ species takes place after more than 30 min of reaction, and then the oxygen moiety of the carbonate species may react with CH$_x$ and carbon species coming from CH$_4$ activation on the Ni sites [62] to form stably CO and H$_2$. Such a mechanism likely occurs on the Ni—La CA as well, however, the presence of large Ni particles easily deactivating by preferential carbon coking hides the synergistic interaction between the small Ni sites and the support interface.

Looking at the data reported in Table 3 it is noteworthy that both Ni catalysts showed higher CH$_4$ and CO$_2$ conversion values, H$_2$ yield and H$_2$/CO ratio at time = 0 at 650 °C than those recorded at 650 °C during the gradient test. These results can be explained taking into account that long run tests have been performed after gradient tests and then an activation
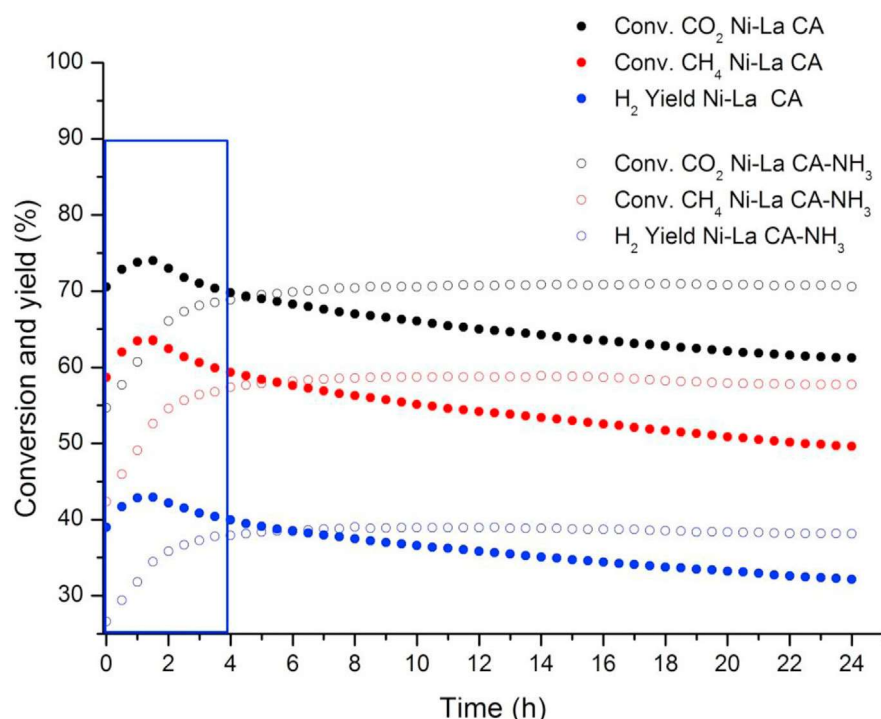
Fig. 10 — DRM long run tests at 650 °C during 24 h for Ni La-CA and Ni—La CA-NH$_3$ catalysts.
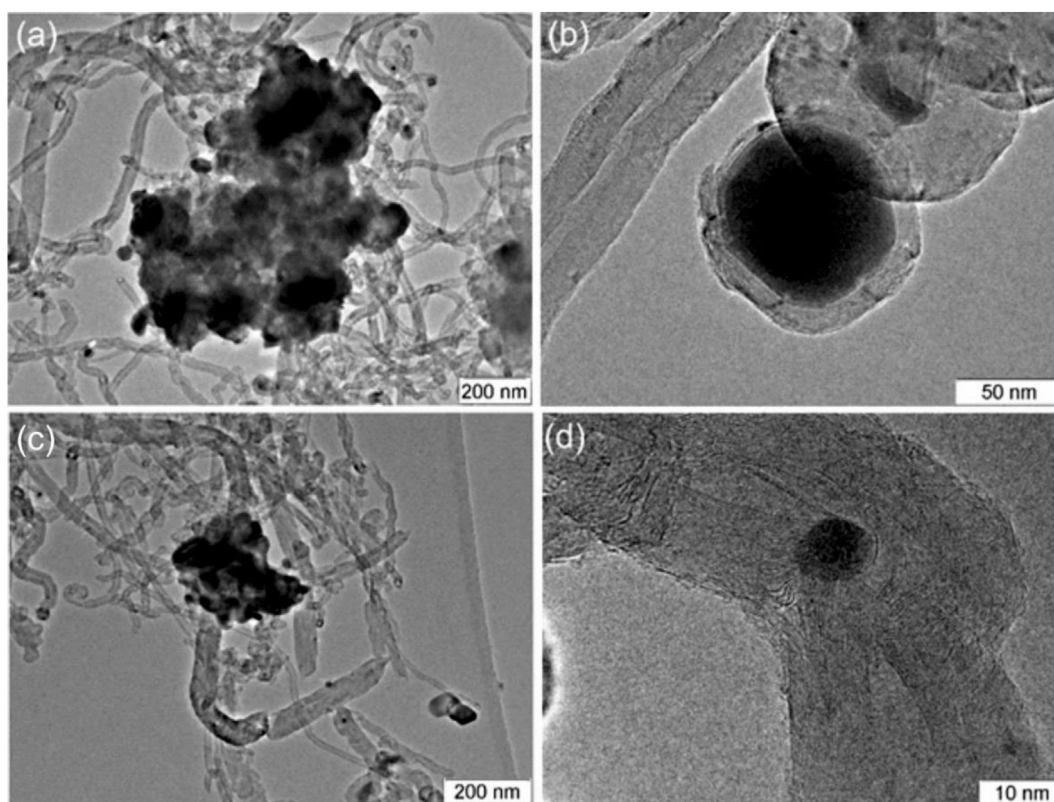
Fig. 11 – TEM HR images of carbon formation after DRM reaction over Ni–La CA (a, b) and Ni–La CA-NH$_3$ (c, d) catalysts.

process occurred with a high extent for Ni–La CA-NH$_3$ as discussed above.

The comparison of DRM catalytic data recorded in the present work with data reported in the literature on similar catalysts (see Table S1) emphasizes the important effect of morphological and structural properties of the samples on their catalytic performances.

Study of spent catalysts after long run test

In order to get insights into the phenomena occurring during the DRM tests, the spent catalysts recovered after long run were analyzed by several techniques. S6 shows the XRD patterns. In both samples, the La$_2$O$_2$CO$_3$ phase was formed along with the C graphite peak of higher intensity in the case of Ni–La CA catalyst (see the enlargement S6 b). Due to the peaks overlapping at ~44.5° 2θ, it is impossible to comment on the metallic Ni sintering.

Fig. S7 shows the data of TGA analysis after the long run test. To confirm the content of carbonates and coke, the TGA analysis was carried out in N$_2$ (a) and air flow (b), respectively. Under N$_2$ flow, the TGA curve of Ni–La CA showed slightly higher weight loss (25.31% *vs* 21.45%) accompanied by higher evolution of CO$_2$ due to the decomposition of La$_2$O$_2$CO$_3$ or La$_2$CO$_5$ phases. Such a slightly higher carbonate content detected for Ni–La CA after the long run suggested a lower consumption of such species during the DRM that could be related to a lower interaction between the Ni active sites and

the support interface that was less effective in favouring oxidation of carbonaceous deposits. Indeed, according to what observed during the TGA under air flow after CH$_4$ test, such a catalyst exhibited high weight loss due to carbon coke oxidation. The weight loss was much higher than that registered for Ni–La CA-NH$_3$ (~53.7% *vs* 10.7%) according to the significant deactivation occurring during the long run. Furthermore, as observed for the previous TGA curves (see S4), the decomposition of coke deposited over Ni–La CA-NH$_3$ occurred at higher temperature than for the Ni–La-CA suggesting again the formation of more crystalline carbon in the former sample.

Fig. 11 illustrates the morphology of the carbon formed on the surface of Ni–La CA (Fig. 11a, b) and Ni–La CA-NH$_3$ (Fig. 11c, d) catalysts after the DRM reaction. TEM images display two types of carbon: filaments and layered carbon with graphene structure. Fig. 11 shows large aggregates of lanthanum oxide packed with carbon and some small nickel particles encapsulated in carbon filaments for Ni–La CA catalyst. Moreover, for this catalyst Fig. 11b displays a large sintered nickel particle with the size of ~80 nm encapsulated by graphene. Conversely, Ni–La CA-NH$_3$ catalyst exhibited small nickel nanoparticles (8–12 nm) and low aggregation of La$_2$O$_3$ particles (Fig. 11c, d).

Fig. S8 represents the Raman spectra of the spent catalysts after the DRM. As previously stated, the relative intensity between the two peaks (I$_D$/I$_G$) gives information about the type of carbon nanotubes and the extent of crystallinity. In the

present figure, the I_D/I_G ratio equals to 1.43 for Ni—La CA and to 1.59 for Ni—La CA-NH₃, respectively. According to the results obtained, the carbon formed over Ni—La CA-NH₃ is more crystalline in comparison with Ni—La-CA.

Conclusions

10%Ni/La₂O₃ catalysts were synthesized by wetness impregnation of lanthana supports prepared using sol-gel citric method with and without NH₃ addition (Ni—La CA-NH₃ and Ni—La CA, respectively) and studied in the dry reforming of methane. Fresh and spent samples were characterized by XRD, TPR, TGA, Raman and TEM HR analyses. The gradient temperature DRM tests (400—800 °C) revealed higher activity for Ni—La CA sample, while the Ni—La CA-NH₃ specimen was more stable during the long run test (650 °C, 24 h), with the former catalyst suffering from the continuous deactivation in the long run DRM test. Different catalytic behaviour of two Ni/La₂O₃ catalysts was explained in terms of structures and phase composition of the supports that affected the nature of Ni-containing phases in the calcined catalysts. The Ni—La CA sample activated methane faster due to different nature of Ni phases, namely, NiO and the mixture of La₃Ni₂O₆ and LaNiO₃ with higher contribution of the latter phase, in comparison with the Ni La CA-NH₃ sample, where La₃Ni₂O₆ was predominantly formed.

The reduction of the Ni La CA-NH₃ sample resulted in the formation of ultrasmall (1—2 nm) Ni NPs strongly interacting with the support as confirmed by the TPR and TEM results. The carbon deposits formed during the reaction were accumulated on the exposed active Ni sites of the Ni—La CA sample limiting its activity and deactivating the catalyst during the long run DRM test. Contrary, the Ni La CA-NH₃ sample featured Ni particles stronger interacting with the support and less exposed to poisoning effect of the active site by carbon. The superior activity of Ni La CA-NH₃ sample was explained by the formation of La₂O₂CO₃ species able to oxidize carbon and an interaction of small Ni particles with the support that maintained high dispersion during the reaction.

Declaration of competing interest

The authors declare that they have no known competing financial interests or personal relationships that could have appeared to influence the work reported in this paper.

Acknowledgements

Appendix A. Supplementary data

Supplementary data to this article can be found online at https://doi.org/10.1016/j.ijhydene.2020.12.026.

REFERENCES

[1] Lavoie JM. Review on dry reforming of methane, a potentially more environmentally-friendly approach to the increasing natural gas exploitation. Front Chem 2014;11:2—81. https://doi.org/10.3389/fchem.2014.00081.

[2] Zhang L, Lian J, Li L, Peng C, Liu W, Xu X, Fang X, Wang Z, Wang X, Peng H. LaNiO₃ nanocube embedded in mesoporous silica for dry reforming of methane with enhanced coking resistance. Microporous Mesoporous Mater 2018;266:189—97. https://doi.org/10.1016/j.micromeso.2018.02.021.

[3] Muraza O, Galadmina A. A review on coke management during dry reforming of methane. Int J Energy Res 2015;39:1196—216. https://doi.org/10.1002/er.3295.

[4] Usman M, Daud WMAW, Abbas HF. Dry reforming of methane: influence of process parameters — a review. Renew Sustain Energy Rev 2015;45:710—44. https://doi.org/10.1016/j.rser.2015.02.026.

[5] Liu H, Wierzbicki D, Debek R, Motak M, Grzybek T, Da Costa P, Gálvez ME. La-promoted Ni-hydrotalcite-derived catalysts for dry reforming of methane at low temperatures. Fuel 2016;182:8—16. https://doi.org/10.1016/j.fuel.2016.05.073.

[6] Pakhare D, Spivey J. A review of dry (CO₂) reforming of methane over noble metal catalysts. Chem Soc Rev 2014;43:7813—37. https://doi.org/10.1039/C3CS60395D.

[7] Arora S, Prasad R. An overview on dry reforming of methane: strategies to reduce carbonaceous deactivation of catalysts. RSC Adv 2016;6:108668—88. https://doi.org/10.1039/C6RA20450C.

[8] Lv J, Wang D, Wang M, Li Y, Jin L, Hu H. Integrated coal pyrolysis with dry reforming of low carbon alkane over Ni/La₂O₃ to improve tar yield. Fuel 2020;266:117092. https://doi.org/10.1016/j.fuel.2020.117092.

[9] Singh RK, Shukla A, Yadav A, Sivakumar Konathala LN, Bal R. Effect of metal-support interaction on activity and stability of Ni-CeO₂ catalyst for partial oxidation of methane. Appl Catal B Environ 2017;202:473—88. https://doi.org/10.1016/j.apcatb.2016.09.060.

[10] Pakhare D, Schwartz V, Abdelsayed V, Haynes D, Shekhawat D, Poston J, Spivey J. Kinetic and mechanistic study of dry (CO₂) reforming of methane over Rh-substituted La₂Zr₂O₇ pyrochlores. J Catal 2014;316:78—92. https://doi.org/10.1016/j.jcat.2014.04.023.

[11] Zhang L, Wang F, Zhu J, Han B, Fan W, Zhao L, Cai W, Li Z, Xu L, Yu H, Shi W. CO₂ reforming with methane reaction over Ni@SiO₂ catalysts coupled by size effect and metal-support interaction. Fuel 2019;256:115954. https://doi.org/10.1016/j.fuel.2019.115954.

[12] Wei Q, Gao X, Liu G, Yang R, Zhang H, Yang G, Yoneyama Y, Tsubaki N. Facile one-step synthesis of mesoporous Ni-Mg-Al catalyst for syngas production using coupled methane reforming process. Fuel 2018;211:1—10. https://doi.org/10.1016/j.fuel.2017.08.093.

[13] Rossetti I, Gallo A, Dal Santo V, Bianchi CL, Nichele V, Signoretto M, Finocchio E, Ramis G, Di Michele A. Nickel catalysts supported over TiO₂, SiO₂ and ZrO₂ for the steam

reforming of glycerol. ChemCatChem 2013;5:294—306. https://doi.org/10.1002/cctc.201200481.

[14] Senseni AZ, Meshkani F, Rezaei M. Steam reforming of glycerol on mesoporous nanocrystalline Ni/Al$_2$O$_3$ catalysts for H$_2$ production. Int J Hydrogen Energy 2016;41:20137—46. https://doi.org/10.1016/j.ijhydene.2016.08.046.

[15] Demsash HD, Mohan R. Steam reforming of glycerol to hydrogen over ceria promoted nickel-alumina catalysts. Int J Hydrogen Energy 2016;41:22732—42. https://doi.org/10.1016/j.ijhydene.2016.10.082.

[16] Charisiou ND, Papageridis KN, Siakavelas G, Tzounis L, Kousi K, Baker MA, Hinder SJ, Sebastian V, Polychronopoulou K, Goul MA. Glycerol steam reforming for hydrogen production over nickel supported on alumina, zirconia and silica catalysts. Top Catal 2017;60(15—16):1—25. https://doi.org/10.1007/s11244-017-0796-y.

[17] Ali Zadeh Sahraei O, al Larachi F, Abatzoglou N, Iliut MC. Hydrogen production by glycerol steam reforming catalyzed by Ni-promoted Fe/Mg-bearing metallurgical wastes. Appl Catal B Environ 2017;219:183—93. https://doi.org/10.1016/j.apcatb.2017.07.039.

[18] Charisiou ND, Siakavelas G, Papageridis KN, Baklavaridis A, Tzounis L, Polychronopoulou K, Goul MA. Hydrogen production via the glycerol steam reforming reaction over nickel supported on alumina and lanthana-alumina catalysts. Int J Hydrogen Energy 2017;42:13039—60. https://doi.org/10.1016/j.ijhydene.2017.04.048.

[19] Thyssen VV, Georgetti F, Assaf EM. Influence of MgO content as an additive on the performance of Ni/MgO-SiO$_2$ catalysts for the steam reforming of glycerol. Int J Hydrogen Energy 2017;42:16979—90. https://doi.org/10.1016/j.ijhydene.2017.05.180.

[20] Bepari S, Pradhan NC, Dalai AK. Selective production of hydrogen by steam reforming of glycerol over Ni/Fly ash catalyst. Catal Today 2017;291:36—46. https://doi.org/10.1016/j.cattod.2017.01.015.

[21] Dang C, Wang H, Yu H, Peng F. Sorption-enhanced steam reforming of glycerol over Ni-Cu-Ca-Al catalysts for producing fuel-cell grade hydrogen. Int J Hydrogen Energy 2017;42:17446—56. https://doi.org/10.1016/j.ijhydene.2017.03.073.

[22] Goula MA, Charisiou ND, Siakavelas G, Tzounis L, Tsiaoussis I, Panagiotopoulou P, Goula G, Yentekakis IV. Syngas production via the biogas dry reforming reaction over Ni supported on zirconia modified with CeO$_2$ or La$_2$O$_3$ catalysts. Int J Hydrogen Energy 2017;42:13724—40. https://doi.org/10.1016/j.ijhydene.2016.11.196.

[23] Nair MM, Kaliaguine S, Kleitz F. Nanocast LaNiO$_3$ perovskites as precursors for the preparation of coke-resistant dry reforming catalysts. ACS Catal 2014;4:3837—46. https://doi.org/10.1021/CS500918C.

[24] Li X, Li Di, Tian H, Zeng L, Zhao Z-J, Gong J. Dry reforming of methane over Ni/La$_2$O$_3$ nanorod catalysts with stabilized Ni nanoparticles. Appl Catal B Environ 2017;202:683—94. https://doi.org/10.1016/j.apcatb.2016.09.071.

[25] Verykios XE. Catalytic dry reforming of natural gas for the production of chemicals and hydrogen. Int J Hydrogen Energy 2003;28:1045—63. https://doi.org/10.1016/S0360-3199(02)00215-X.

[26] Melchor-Hernandez C, Gymez-Cortes A, Diaz G. Hydrogen production by steam reforming of ethanol over nickel supported on La-modified alumina catalysts prepared by sol—gel. Fuel 2013;107:828—35. https://doi.org/10.1016/j.fuel.2013.01.047.

[27] Khoja AH, Tahir M, Saidina Amin NA. Evaluating the performance of a Ni catalyst supported on La$_2$O$_3$-MgAl$_2$O$_4$ for dry reforming of methane in a packed bed dielectric barrier discharge plasma reactor. Energy Fuels 2019;33:11630—47. https://doi.org/10.1021/acs.energyfuels.9b02236.

[28] Khoja AH, Tahir M, Saidina Amin NA. Process optimization of DBD plasma dry reforming of methane over Ni/La$_2$O$_3$-MgAl$_2$O$_4$ using multiple response surface methodology. Int J Hydrogen Energy 2019;44:11774—87. https://doi.org/10.1016/j.ijhydene.2019.03.059.

[29] Khoja AH, Tahir M, Amin NAS, Javed A, Mehran MT. Kinetic study of dry reforming of methane using hybrid DBD plasma reactor over La$_2$O$_3$ co-supported Ni/MgAl$_2$O$_4$ catalyst. Int J Hydrogen Energy 2020;45:12256—71. https://doi.org/10.1016/j.ijhydene.2020.02.200.

[30] Xu L, Liu W, Zhang X, Tao L, Xia L, Xu X, Song J, Zhou W, Fang X, Wang X. Ni/La$_2$O$_3$ catalysts for dry reforming of methane: insights into the factors improving the catalytic performance. ChemCatChem 2019;11:2887—99. https://doi.org/10.1002/cctc.201900331.

[31] Jahangiri A, Pahlavanzadeh H, Aghabozorg H. Synthesis, characterization and catalytic study of Sm doped LaNiO$_3$ nanoparticles in reforming of methane with CO$_2$ and O$_2$. Int J Hydrogen Energy 2012;37:9977—84. https://doi.org/10.1016/j.ijhydene.2012.03.128.

[32] Soares MD, Carvalho ME, Melo Jorge A, Gomes RA, Silva CM, Rangel MI. High surface area LaNiO$_3$ electrodes for oxygen electrocatalysis in alkaline media. J Appl Electrochem 2012;42:325—32. https://doi.org/10.1007/s10800-012-0399-z.

[33] Franchini CA, Aranzaez W, Duarte de Farias AM, Pecchi G, Fraga MA. Ce-substituted LaNiO$_3$ mixed oxides as catalyst precursors for glycerol steam reforming. Appl Catal B Environ 2014;147:193—202. https://doi.org/10.1016/j.apcatb.2013.08.036.

[34] Lin KH, Wang CB, Chien SH. Catalytic performance of steam reforming of ethanol at low temperature over LaNiO$_3$ perovskite. Int J Hydrogen Energy 2013;38:3226—32. https://doi.org/10.1016/j.ijhydene.2013.01.005.

[35] Galal A, Atta NF, Ali SM. Optimization of the synthesis conditions for LaNiO$_3$ catalyst by microwave assisted citrate method for hydrogen production. Appl Catal A 2011;409—410:202—8. https://doi.org/10.1016/j.apcata.2011.10.005.

[36] Yang J, Li R, Zhou J, Li X, Zhang Y, Long Y, Li Y. Synthesis of LaMO$_3$ (M = Fe, Co, Ni) using nitrate or nitrite molten salts. J Alloys Compd 2010;508:301—8. https://doi.org/10.1016/j.jallcom.2010.08.073.

[37] Iwasaki T, Shimamura Y, Makino Y, Watano S. Mechanochemically assisted synthesis and visible light photocatalytic properties of lanthanum nickel oxide nanoparticles. Optik 2016;127:9081—7. https://doi.org/10.1016/j.ijleo.2016.06.125.

[38] Pereñíguez R, González-Dela Cruz VM, Holgado JP, Caballero A. Synthesis and characterization of a LaNiO$_3$ perovskite as precursor for methane reforming reactions catalysts. Appl Catal B: Environ 2010;93(3—4):346—53. https://doi.org/10.1016/j.apcatb.2009.09.040.

[39] Granger P, Parvulescu VI, Kaliaguine S, Prellier W. Perovskites and related mixed oxides: concepts and applications. Wiley Blackwell; 2016. https://doi.org/10.1002/9783527686605.

[40] Bonmassar N, Bekheet MF, Schlicker L, Gili A, Gurlo A, Doran A, Gao Y, Heggen M, Bernardi J, Klötzer B, Penner S. In situ-determined catalytically active state of LaNiO$_3$ in methane dry reforming. ACS Catal 2020;10:1102—12. https://doi.org/10.1021/acscatal.9b03687.

[41] Sierra Gallego Germán, Mondragón Fanor, Jean-Michel Tatibouët Joël Barraulta, Batiot-Dupeyrat Catherine. CO$_2$ reforming of CH$_4$ over La—Ni based perovskite precursors.

Appl Catal A 2006;311:164—71. https://doi.org/10.1016/j.apcata.2006.06.024.

[42] Wu G, Li S, Zhang C, Wang T, Gong J. Glycerol steam reforming over perovskite-derived nickel-based catalysts. Appl Catal B Environ 2014;144:277—85. https://doi.org/10.1016/j.apcatb.2013.07.028.

[43] Licci F, Turilli G, Ferro P, Ciccarone A. Low-temperature synthesis and properties of $LaMnO_{3\pm d}$ and $La_{0.67}R_{0.33}MnO_{3\pm d}$ (R = Ca, Sr, Ba) from citrate precursors. J Am Ceram Soc 2003;86:413—9. https://doi.org/10.1111/j.1151-2916.2003.tb03314.x.

[44] Predoana L, Jitianu A, Malic B, Zaharescu M. Study of the gelling process in the La-Co-citric acid system. J Am Ceram Soc 2012;95(3):1068—76. https://doi.org/10.1111/j.1551-2916.2011.04965.x.

[45] Vanhoyland G, Pagnaer J, D'Haen J, Mullens S, Mullens J. Characterization and structural study of lanthanum citrate trihydrate $[La(C_6H_5O_7)(H_2O)_2]\cdot H_2O$. J Solid State Chem 2005;178(1):166—71. https://doi.org/10.1016/j.jssc.2004.10.042.

[46] Chen M-L, Gao S, Zhou Z-H. Isolations and characterization of highly water-soluble dimeric lanthanide citrate and malate with ethylenediaminetetraacetate. Dalton Trans 2012;41:1202—9. https://doi.org/10.1039/C1DT11466B.

[47] Bernal S, Botana FJ, Garcia R, Ramirez F, Rodríguez-Izquierdo JM. Solid state chemistry of the preparation of lanthana-supported metal catalysts — study of the impregnation step. J Mater Sci 1987;22(10):3793—800. https://doi.org/10.1007/BF01161496.

[48] Belik Y, Kharlamova T, Vodyankin A, Svetlichnyi V, Vodyankina O. Mechanical activation for soft synthesis of bismuth silicates. Ceram Int 2020;46(8):10797—806. https://doi.org/10.1016/j.ceramint.2020.01.090.

[49] Egorova SR, Mukhamed'yarova AN, Kurbangaleeva AZ, Zhang Yuqing, Lamberov AA. Formation of closed mesopores in boehmite during the phase transformation of gibbsite under hydrothermal conditions. React Kinet Mech Catal 2018;125:873—85. https://doi.org/10.1007/s11144-018-1431-z.

[50] Sutthiumporn K, Kawi S. Promotional effect of alkaline earth over $Ni-La_2O_3$ catalyst for CO_2 reforming of CH_4: role of surface oxygen species on H_2 production and carbon suppression international journal of hydrogen energy. Int J Hydrogen Energy 2011;36:14435—46. https://doi.org/10.1016/j.ijhydene.2011.08.022.

[51] Oliveira Angelo AS, Rodolfo L, Medeiros BA, Figueredo Gilvan P, Macedo Heloısa P, Braga Renata M, Maziviero Fernando V, Melo Marcus AF, Melo Dulce MA, Vieira Marcela M. One-step synthesis of $LaNiO_3$ with chitosan for dry reforming of methane. Int J Hydrogen Energy 2018:1—9. https://doi.org/10.1016/j.ijhydene.2018.03.212.

[52] Xu X, Li L, Yu F, Peng H, Fang X, Wang X. Mesoporous high surface area NiO synthesized with soft templates: remarkable for catalytic CH_4 deep oxidation. J Mol Catal 2017;441:81—91. https://doi.org/10.1016/j.mcat.2017.08.005.

[53] Rabelo-Neto RC, Sales HBE, Inocencio CVM, Varga E, Oszko A, Erdohelyi A, Noronha FB, Mattos V. CO_2 reforming of methane over supported $LaNiO_3$ perovskite-type oxides. Appl Catal B Environ 2018;221:349—61. https://doi.org/10.1016/j.apcatb.2017.09.022.

[54] Poltavets VV, Lokshin KA, Dikmen S, Croft Mk, Egami T, Greenblatt M. $La_3Ni_2O_6$: a new double T'-type nickelate with infinite $Ni^{1+/2+}O_2$ layers. J Am Chem Soc 2006;128:9050—1. https://doi.org/10.1021/ja063031o.

[55] Kawi S, Kathiraser Y, Ni J, Oemar U, Li Z. Progress in synthesis of highly active and stable nickel-based catalysts for carbon dioxide reforming of methane. ChemSusChem 2015;8(21):3556—75. https://doi.org/10.1002/cssc.201500390.

[56] Montero C, Ochoa A, Castaño P, Bilbao J, Gayubo AG. Monitoring Ni^0 and coke evolution during the deactivation of a $Ni/La_2O_3-\alpha Al_2O_3$ catalyst in ethanol steam reforming in a fluidized bed. J Catal 2015;331:181—92. https://doi.org/10.1016/j.jcat.2015.08.005.

[57] Zhang J, Li F. Coke-resistant $Ni@ SiO_2$ catalyst for dry reforming of methane. Appl Catal B Environ 2015;176—177:513—21. https://doi.org/10.1016/j.apcatb.2015.04.039.

[58] Nikoo MK, Amin NAS. Thermodynamic analysis of carbon dioxide reforming of methane in view of solid carbon formation. Fuel Process Technol 2011;92:678—91. https://doi.org/10.1016/j.fuproc.2010.11.027.

[59] Horváth A, Guczi L, Kocsonya A, Sáfrán G, La Parola V, Liotta LF, Pantaleo G, Venezia AM. Sol-derived $AuNi/MgAl_2O_4$ catalysts: formation, structure and activity in dry reforming of methane. Appl Catal A Gen 2013;468:250—9. https://doi.org/10.1016/j.apcata.2013.08.053.

[60] Wu H, Pantaleo G, La Parola V, Venezia AM, Collard X, April C, Liotta LF. Bi- and trimetallic Ni catalysts over Al_2O_3 and $Al_2O_3-MO_x$ (M=Ce or Mg) oxides for methane dry reforming: Au and Pt additive effects. Appl Catal B Environ 2014;156—157:350—61. https://doi.org/10.1016/j.apcatb.2014.03.018.

[61] Mesrar F, Kacimi M, Liotta LF, Puleo F, Ziyad M. Syngas production from dry reforming of methane over Ni/perlite catalysts: effect of zirconia and ceria impregnation. Int J Hydrogen Energy 2018;43:17142—55. https://doi.org/10.1016/j.ijhydene.2018.07.104.

[62] Papadopoulou C, Matralis H, Verykios X. Utilization of biogas as a renewable carbon source: dry reforming of methane. In: Catalysis for alternative energy generation; 2012. p. 57—127. Chapter 39.